Electronic Supplementary Material (ESI) for Journal of Materials Chemistry A.

Supplementary Information for

Multifunctional long-lived catalysts for direct hydrogenative conversion of CO_2 to liquid hydrocarbons with upscaling C_{5+} productivity

Yongseok Kim, Yohan Song, Yuhwan Kim, and Kyungsu Na*

Department of Chemistry, Chonnam National University, 77 Yongbong-ro, Buk-gu, Gwangju 61186, Republic of Korea

*To whom correspondence should be addressed:

E-mail (Kyungsu Na) kyungsu_na@chonnam.ac.kr

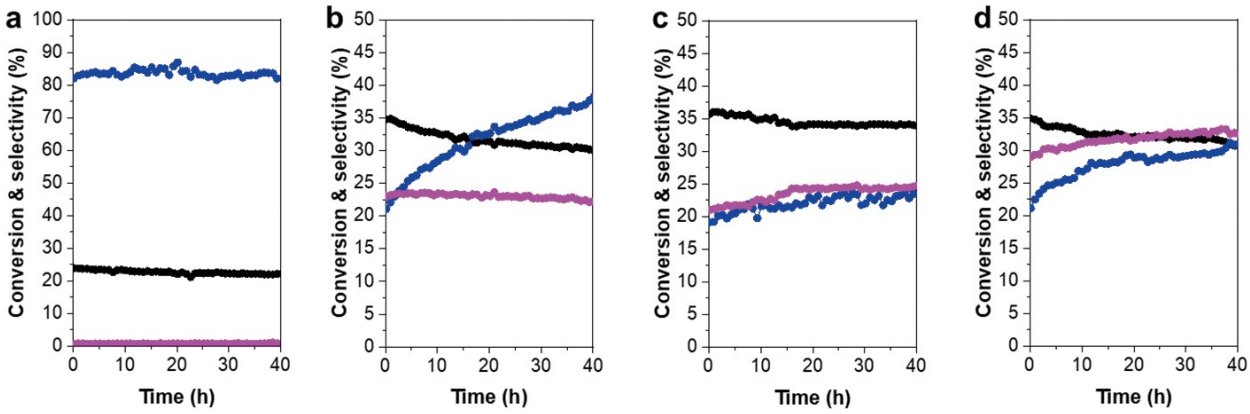

Fig. S1 Reaction profiles of the (a) $CuAl_2O_4$ (entry 1), (b) 9Fe/$CuAl_2O_4$ (entry 2), (c) 22Fe/$CuAl_2O_4$ (entry 3), and (d) 50Fe/$CuAl_2O_4$ (entry 4) catalysts for the 40 h CO_2 hydrogenation reaction. The CO_2 conversion (black dots), CO selectivity (blue dots), and CH_4 selectivity (pink dots) are provided.

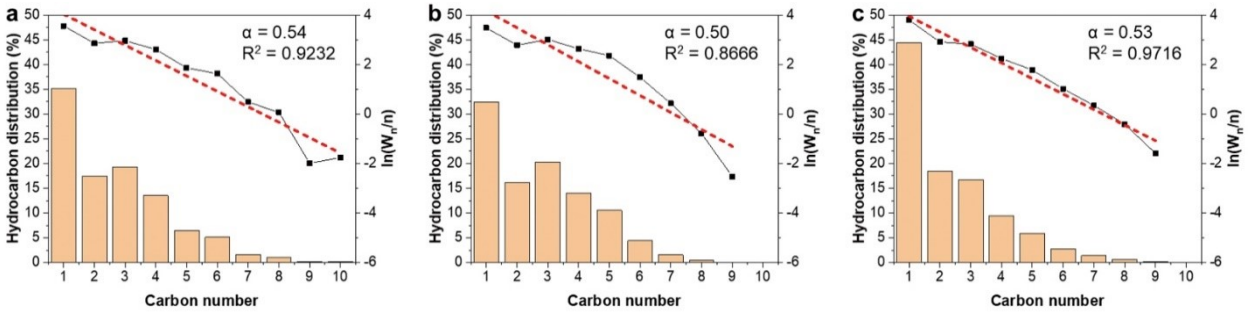

Fig. S2 Hydrocarbon distributions obtained using the (a) 9Fe/$CuAl_2O_4$ (entry 2), (b) 22Fe/$CuAl_2O_4$ (entry 3), and (c) 50Fe/$CuAl_2O_4$ (entry 4) catalysts, with the corresponding Anderson-Schultz-Flory plots (right y-axis) that provide the chain growth probability (α).

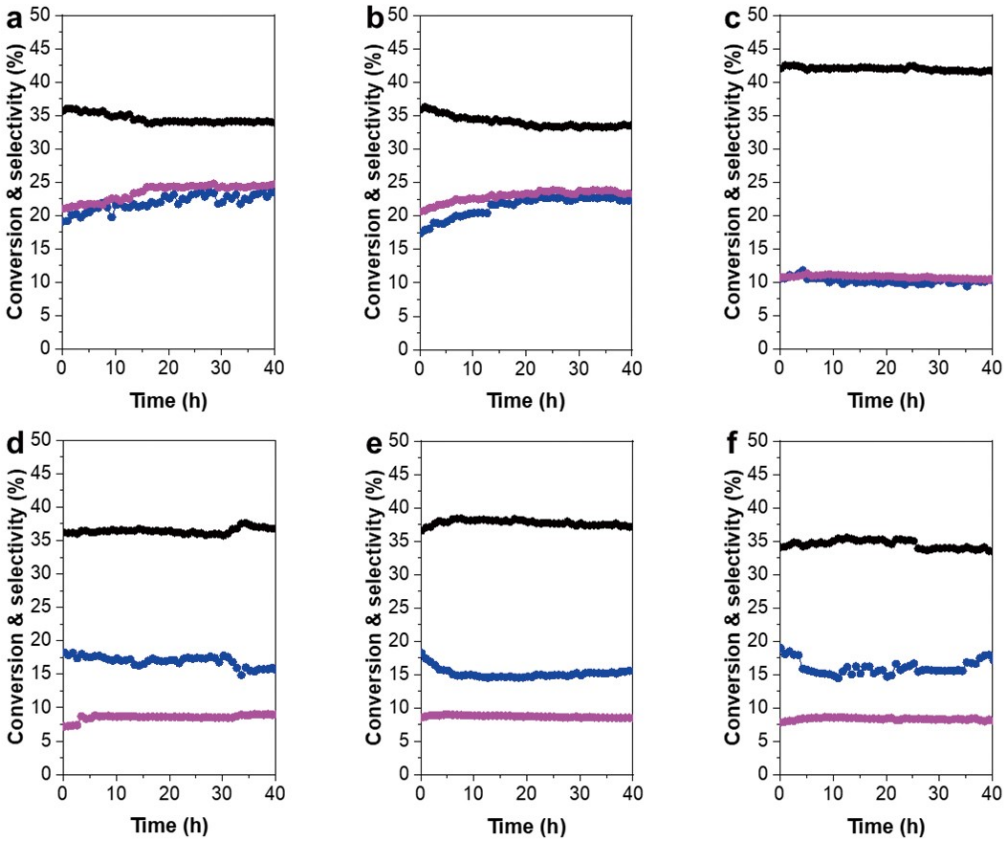

Fig. S3 Reaction profiles of the (a) 22Fe/$CuAl_2O_4$ (entry 3), (b) 22Fe0.8K/$CuAl_2O_4$ (entry 5), (c) 22Fe3K/$CuAl_2O_4$ (entry 6), (d) 22Fe7K/$CuAl_2O_4$ (entry 7), (e) 22Fe15K/$CuAl_2O_4$ (entry 8), and (f) 22Fe22K/$CuAl_2O_4$ (entry 9) catalysts for the 40 h CO_2 hydrogenation reaction. The CO_2 conversions (black dots), CO selectivities (blue dots), and CH_4 selectivities (pink dots) are provided.

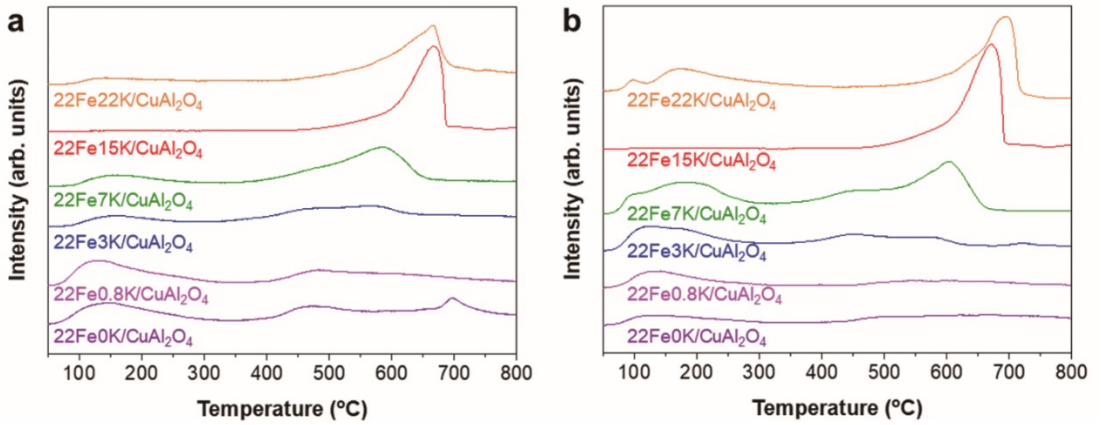

Fig. S4 (a) CO_2-TPD-MS and (b) NH_3-TPD-MS of the 22Fe/$CuAl_2O_4$ and K-promoted catalysts. 22Fe/$CuAl_2O_4$ (violet), 22Fe0.8K/$CuAl_2O_4$ (pink), 22Fe3K/$CuAl_2O_4$ (blue), 22Fe7K/$CuAl_2O_4$ (green), 22Fe15K/$CuAl_2O_4$ (red), and 22Fe22K/$CuAl_2O_4$ (orange) (listed from the bottom to the top).

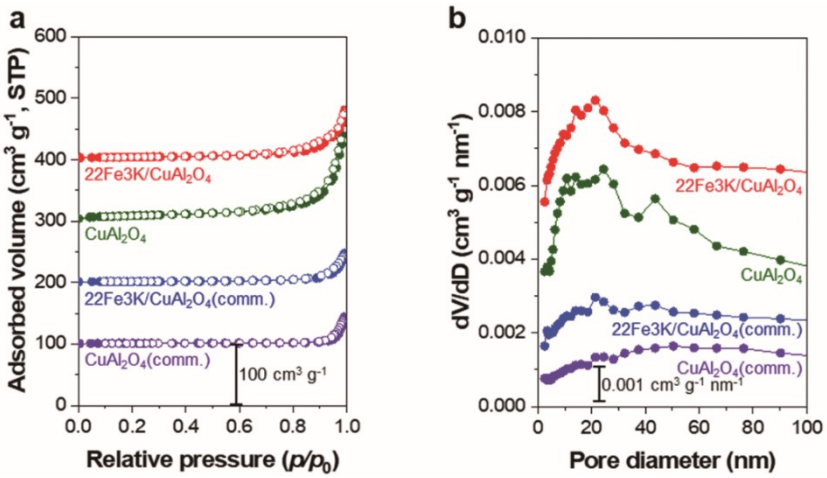

Fig. S5 (a) N_2 adsorption isotherms of 22Fe3K/$CuAl_2O_4$ (red) and $CuAl_2O_4$ (green) having a mesoporous structure in comparison with 22Fe3K/$CuAl_2O_4$ (blue) and $CuAl_2O_4$ (purple) without having a mesoporous structure (from top to bottom), and (b) their corresponding pore size distributions derived from the adsorption branches in (a) using the BJH algorithm.

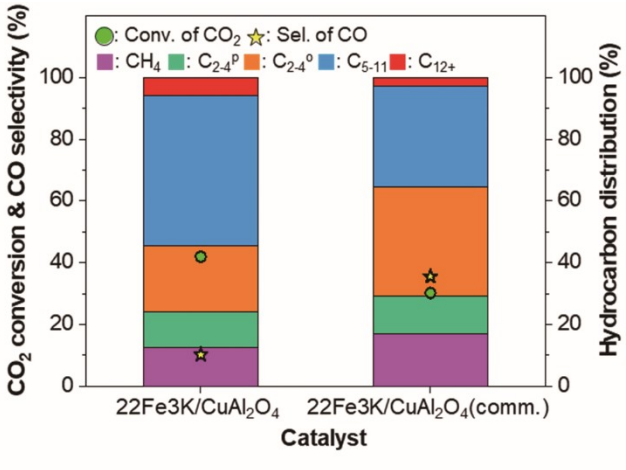

Fig. S6 Comparison of catalytic performance of 22Fe3K/$CuAl_2O_4$ and 22Fe3K/$CuAl_2O_4$(comm.) in the 40 h CO_2 hydrogenation reaction. The CO_2 conversions, CO selectivity, and hydrocarbon distributions are also listed in Table S3 (reaction condition: 320 °C, 3.0 MPa, H_2:CO_2 = 3:1, GHSV = 10 000 mL g_{cat}^{-1} h^{-1}).

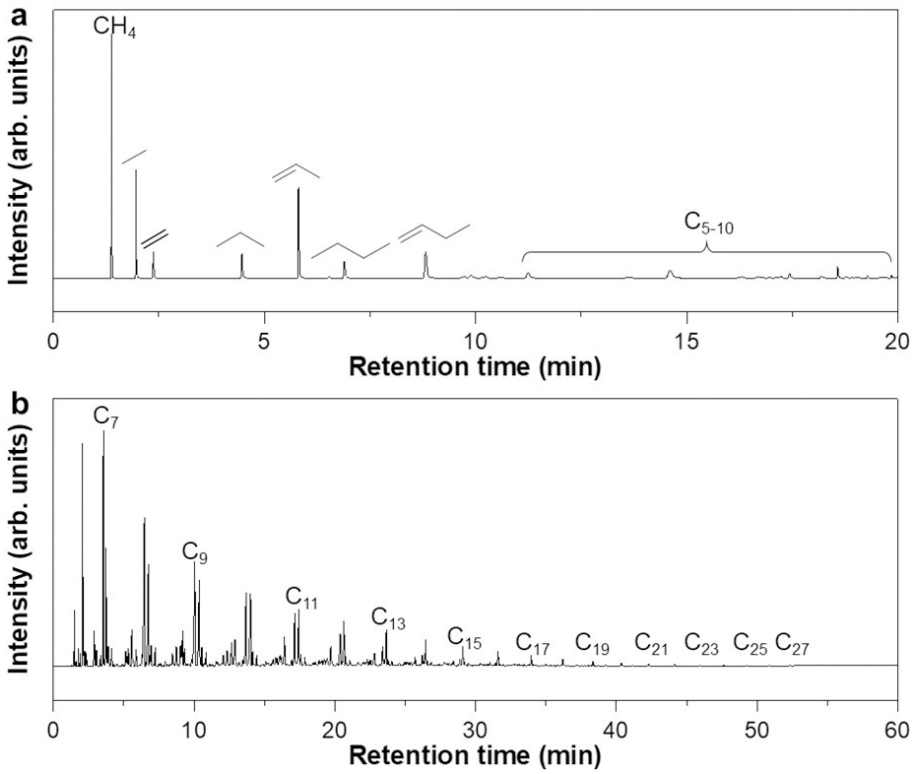

Fig. S7 GC FID chromatograms of the (a) gaseous and (b) liquid products collected in the cold trap during the 40 h reaction in the presence of 22Fe3K/$CuAl_2O_4$ (entry 6).

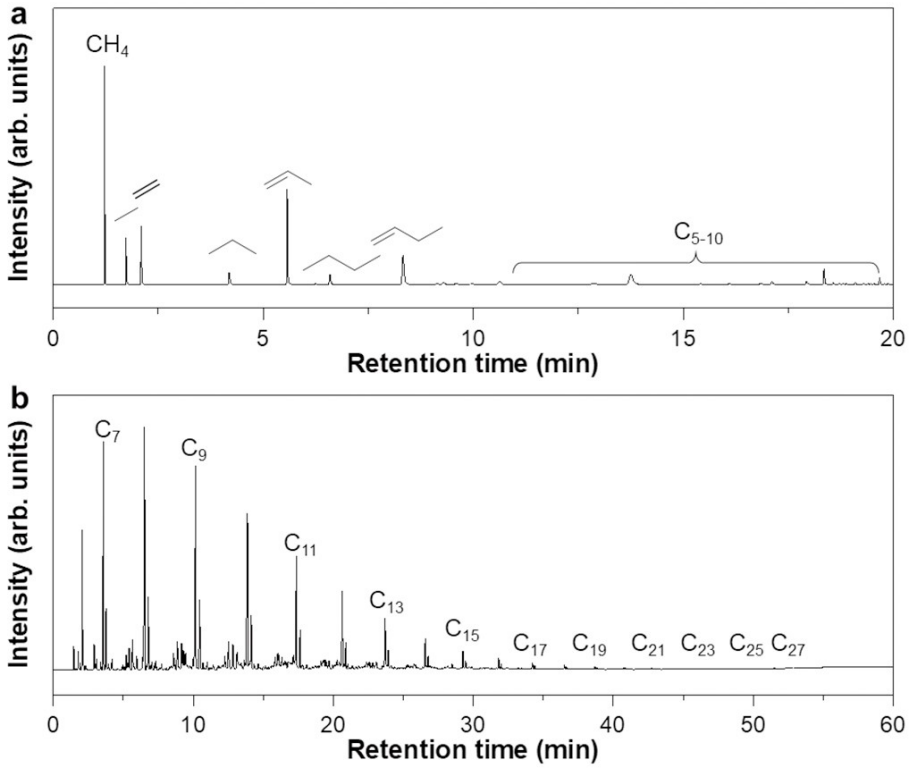

Fig. S8 GC-FID chromatograms of the (a) gaseous and (b) liquid products collected by the cold trap during the 40 h reaction in the presence of 22Fe7K/$CuAl_2O_4$ (entry 7).

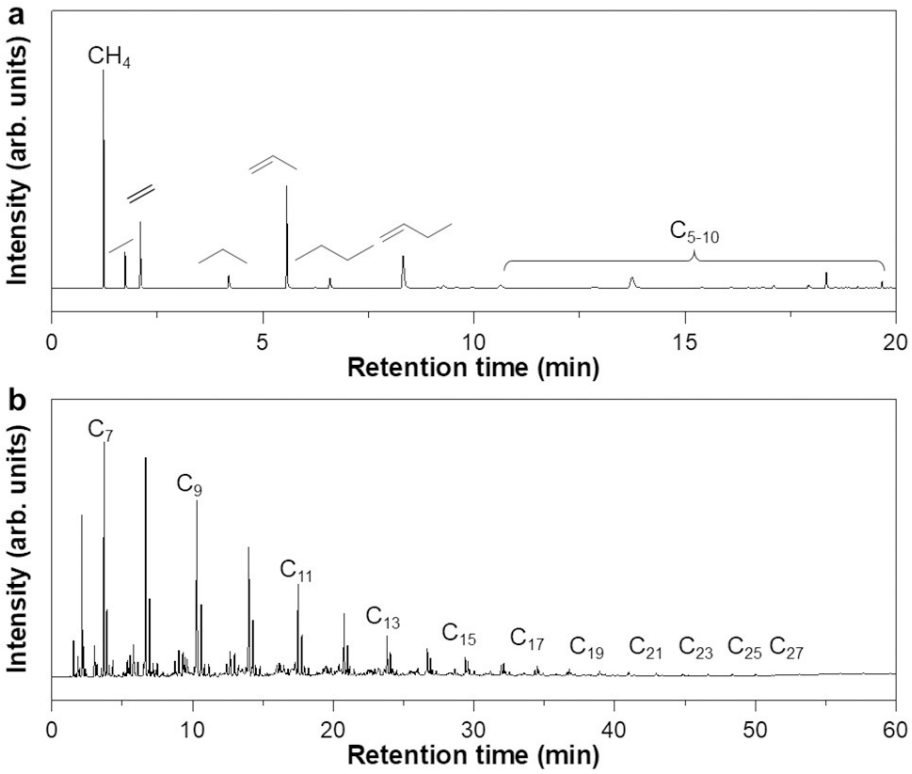

Fig. S9 GC-FID chromatograms of the (a) gaseous and (b) liquid products collected by the cold trap during the 40 h reaction in the presence of 22Fe15K/$CuAl_2O_4$ (entry 8).

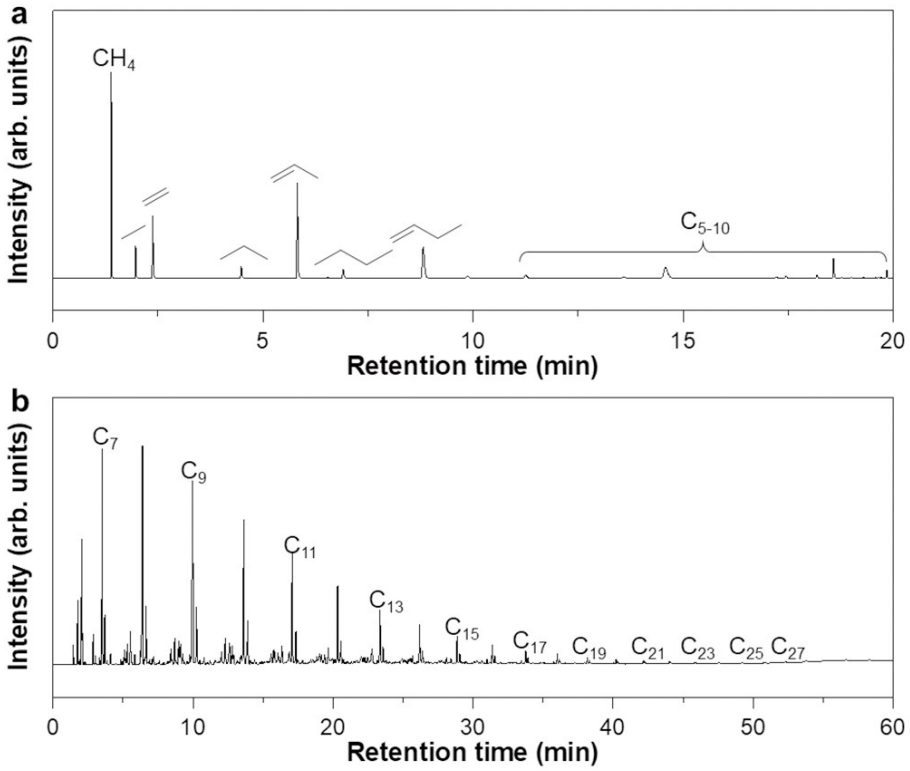

Fig. S10 GC-FID chromatograms of the (a) gaseous and (b) liquid products collected by the cold trap during the 40 h reaction in the presence of 22Fe22K/$CuAl_2O_4$ (entry 9).

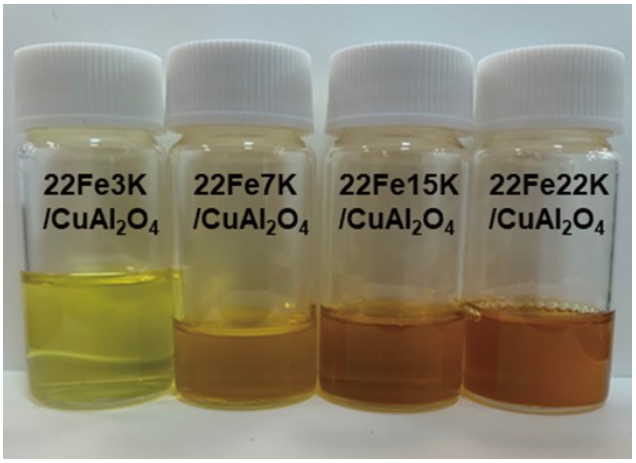

Fig. S11 Photo of the liquid-phase products collected by the cold trap during the 40 h CO_2 hydrogenation reaction performed in the presence of 22Fe3K/$CuAl_2O_4$ (entry 6), 22Fe7K/$CuAl_2O_4$ (entry 7), 22Fe15K/$CuAl_2O_4$ (entry 8), and 22Fe22K/$CuAl_2O_4$ (entry 9) (from left to right).

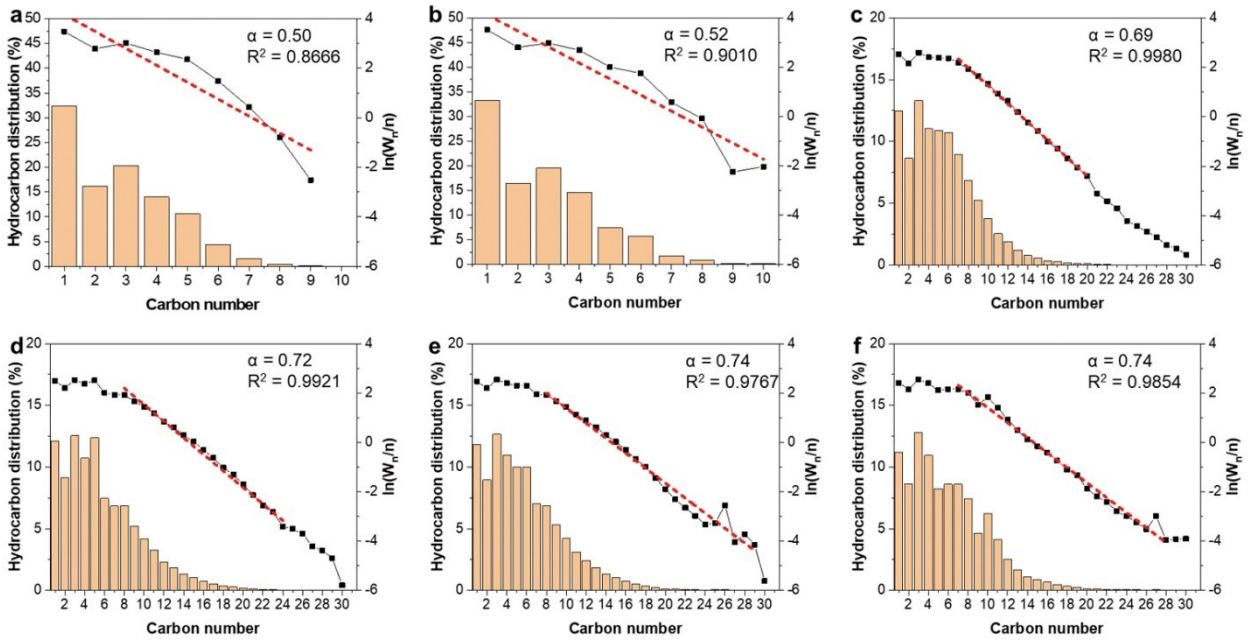

Fig. S12 Hydrocarbon distributions of the (a) 22Fe/$CuAl_2O_4$ (entry 3), (b) 22Fe0.8K/$CuAl_2O_4$ (entry 5), (c) 22Fe3K/$CuAl_2O_4$ (entry 6), (d) 22Fe7K/$CuAl_2O_4$ (entry 7), (e) 22Fe15K/$CuAl_2O_4$ (entry 8), and (f) 22Fe22K/$CuAl_2O_4$ (entry 9) catalysts with their corresponding Anderson-Schultz-Flory plots (right y-axis) providing the chain growth probability (α).

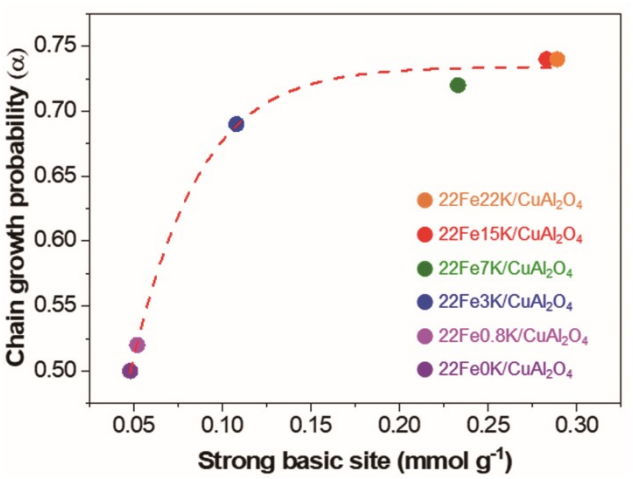

Fig. S13 Correlation graph between amount of strong basic sites of the catalysts with different K loadings (x-axis) and chain growth probability (α) (y-axis).

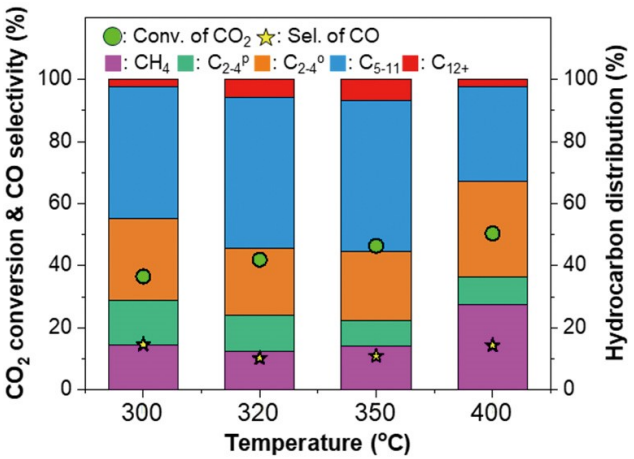

Fig. S14 Effect of the reaction temperature on the catalytic performance of the 22Fe3K/$CuAl_2O_4$ catalyst in the 40 h CO_2 hydrogenation reaction. The CO_2 conversions, CO selectivity, and hydrocarbon distributions are also listed in Table S4.

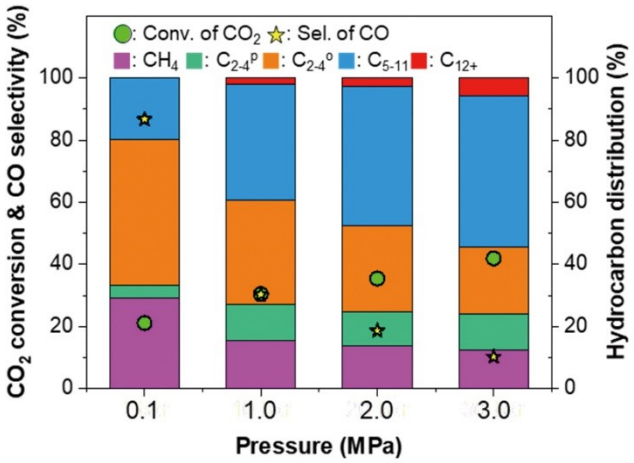

Fig. S15 Effect of the reaction pressure on the catalytic performance of the 22Fe3K/$CuAl_2O_4$ catalyst in the 40 h CO_2 hydrogenation reaction. The CO_2 conversions, CO selectivity, and hydrocarbon distributions are also listed in Table S5.

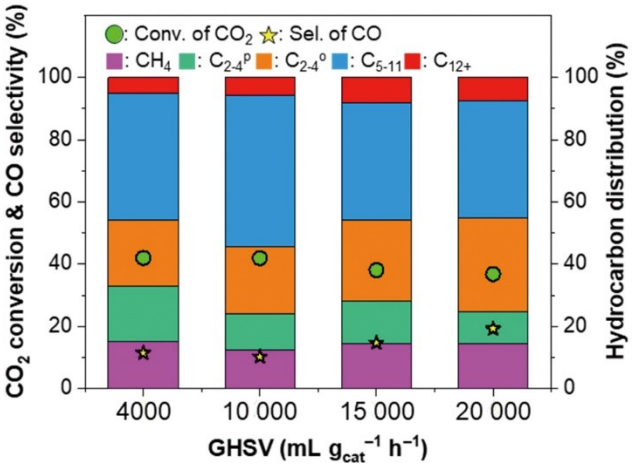

Fig. S16 Effect of the GHSV on the catalytic performance of the 22Fe3K/$CuAl_2O_4$ catalyst in the 40 h CO_2 hydrogenation reaction. The CO_2 conversions, CO selectivity, and hydrocarbon distributions are also listed in Table S6.

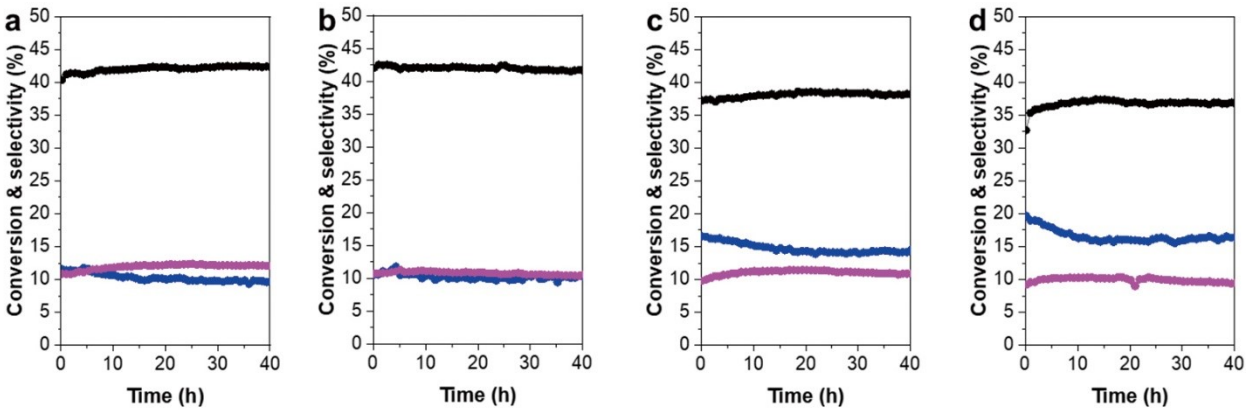

Fig. S17 Reaction profiles of the 22Fe3K/$CuAl_2O_4$ catalyst for the 40 h CO_2 hydrogenation reaction. The CO_2 conversions (black dots), CO selectivity (blue dots), and CH_4 selectivity (pink dots) are provided as a function of the GHSV. (a) 4000, (b) 10 000, (c) 15 000, and (d) 20 000 mL g_{cat}^{-1} h^{-1}.

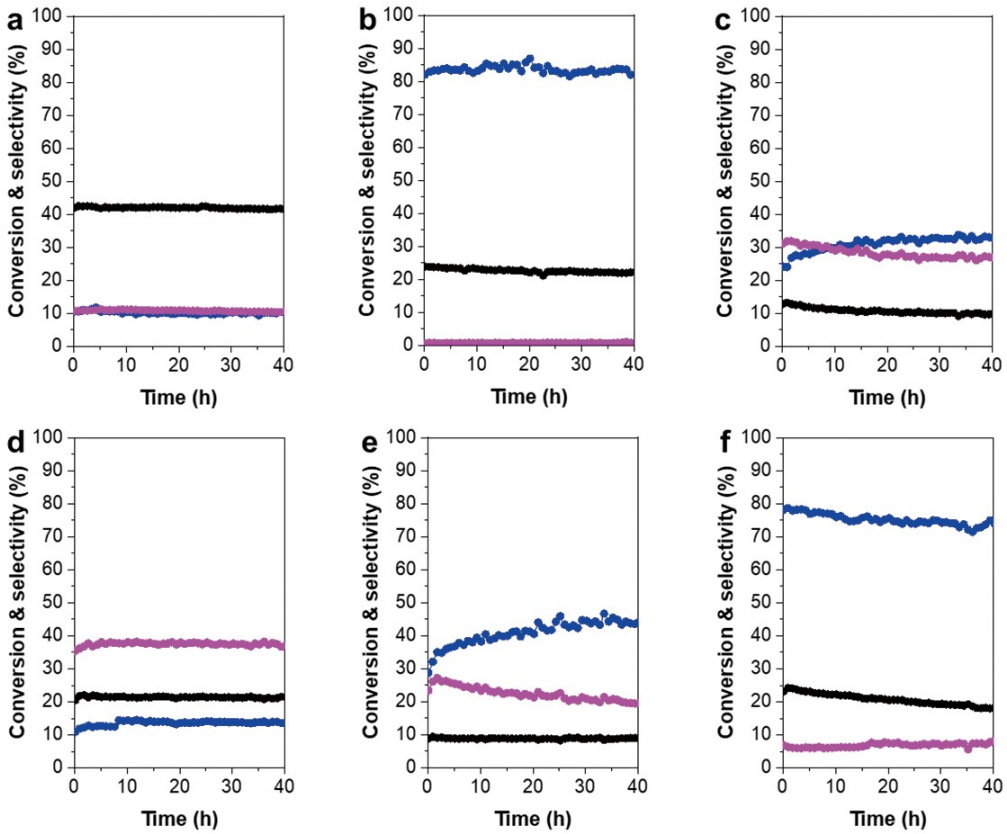

Fig. S18 Reaction profiles of the (a) 22Fe3K/$CuAl_2O_4$, (b) $CuAl_2O_4$, (c) 22Fe/SiO_2, (d) Fe_2O_3, (e) 22Fe3K/SiO_2, and (F) physically mixed 22Fe3K/SiO_2+$CuAl_2O_4$ (P.M.) catalysts for the 40 h CO_2 hydrogenation reaction. The CO_2 conversions (black dots), CO selectivity (blue dots), and CH_4 selectivity (pink dots) are provided.

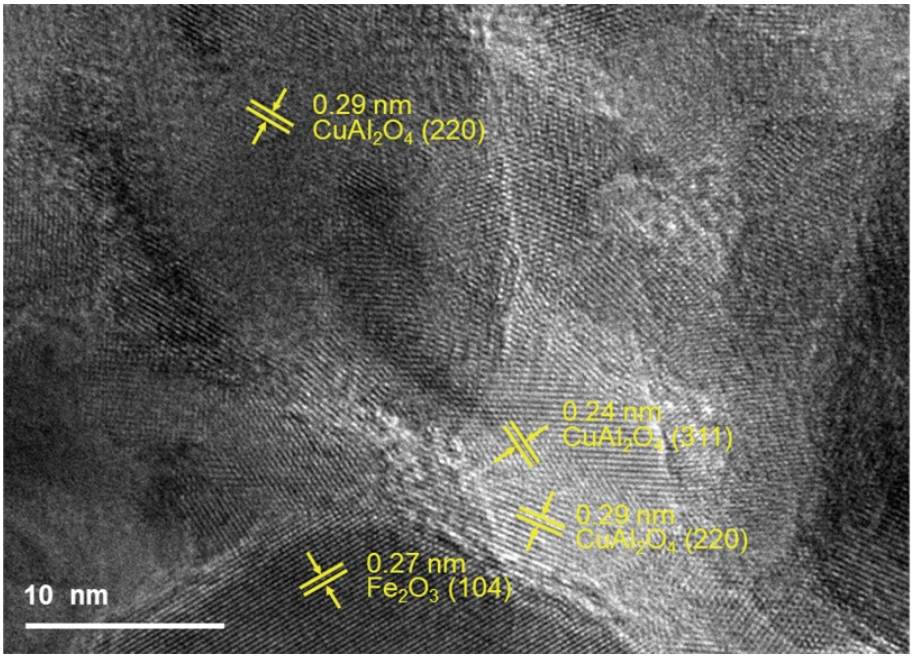

Fig. S19 Magnified HR-TEM image of Fig. 3c showing the distinguishable lattice planes of $CuAl_2O_4$ (220), $CuAl_2O_4$ (311), and Fe_2O_3 (104) that interact on an atomic length scale.

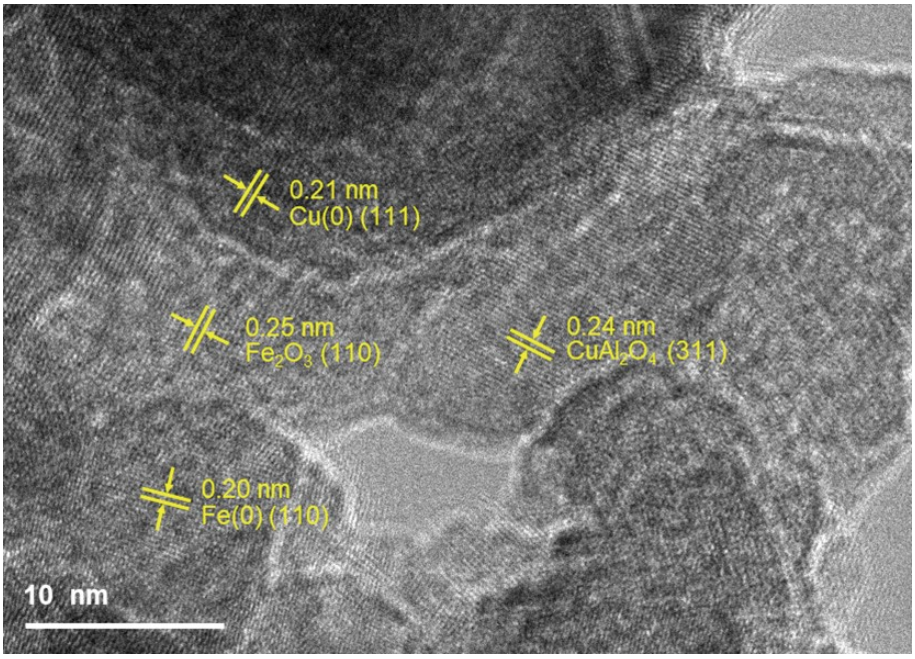

Fig. S20 Magnified HR-TEM image of Fig. 3g showing the distinguishable lattice planes of $CuAl_2O_4$ (311), Cu(0) (111), and Fe(0) (110) that interact on an atomic length scale.

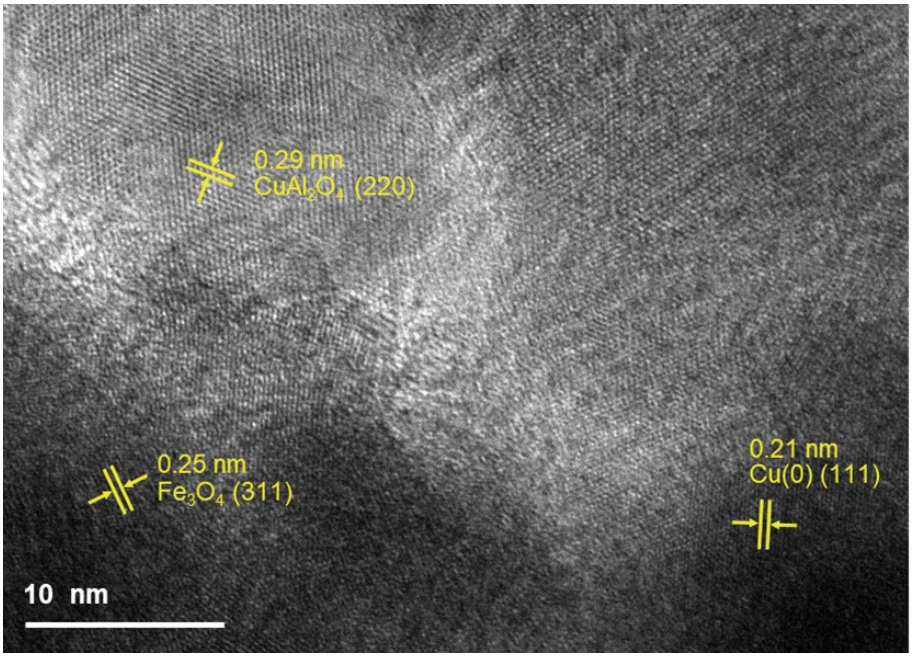

Fig. S21 Magnified HR-TEM image of Fig. 3j showing the distinguishable lattice planes of $CuAl_2O_4$ (220), Cu(0) (111), and Fe_3O_4 (311) that interact on an atomic length scale.

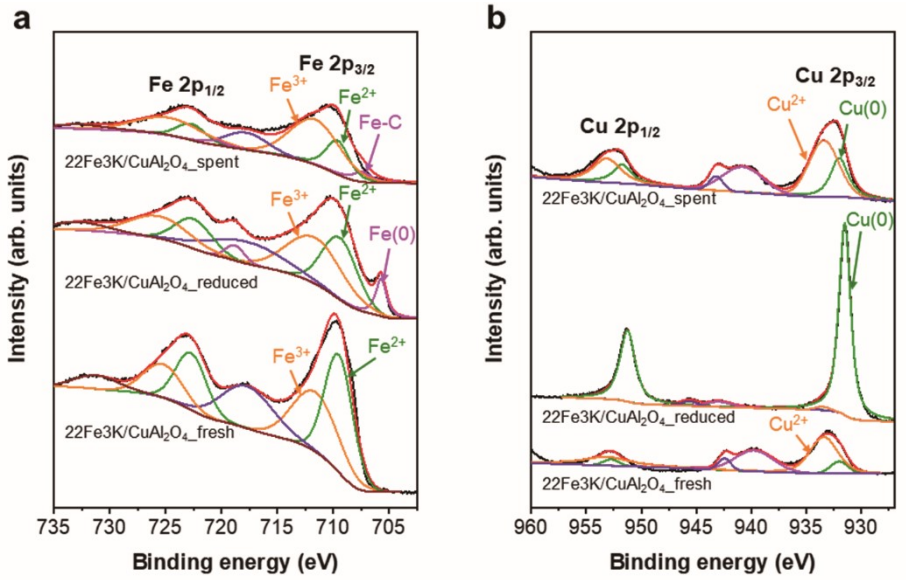

Fig. S22 XPS spectra of 22Fe3K/$CuAl_2O_4$ catalysts in a fresh form (bottom), a reduced form by H_2 pretreatment (middle), and a spent form after reaction (top), showing the (a) Fe 2p and (b) Cu 2p regions separately. The XPS profile in black color is the experimental data, the XPS profiles in orange, green and purple colors are the deconvoluted peaks, and the XPS profile in red color is the fitted profile from the deconvoluted peaks.

Table S1 Elemental composition of the K-containing 22Fe/$CuAl_2O_4$ catalysts determined by ICP–OES.

Sample	Fe (wt.%)	K (wt.%)	Cu (wt.%)	Al (wt.%)
$CuAl_2O_4$	0.0	0.0	39.4	31.3
22Fe0K/$CuAl_2O_4$	24.1	0.0	28.0	21.8
22Fe0.8K/$CuAl_2O_4$	24.9	0.7	27.7	21.7
22Fe3K/$CuAl_2O_4$	24.1	2.7	26.9	21.0
22Fe7K/$CuAl_2O_4$	23.5	6.2	25.6	19.5
22Fe15K/$CuAl_2O_4$	24.8	13.5	22.5	17.8
22Fe22K/$CuAl_2O_4$	22.9	19.6	19.9	16.0

Table S2 Comparison of BET surface areas (S_{BET}) and total pore volumes (V_p).

Sample	S_{BET} ($m^2\ g^{-1}$)	V_p ($cm^3\ g^{-1}$)
$CuAl_2O_4$	31	0.23
22Fe3K/$CuAl_2O_4$	15	0.11
$CuAl_2O_4$(comm.)[a]	4	0.07
22Fe3K/$CuAl_2O_4$(comm.)[a]	6	0.07

[a]Commercially available copper aluminum oxide purchased from Alfa Aesar

Table S3 Comparison of the catalytic performance of 22Fe3K/$CuAl_2O_4$ and 22Fe3K/$CuAl_2O_4$(comm.) as shown in Fig. S6, showing the effect of mesoporous structure.

Catalyst	Temp. (°C)	P (MPa)	GHSV (mL g_{cat}^{-1} h^{-1})	CO_2 conv. (%)	CO sel. (%)	Hydrocarbon distribution (Excluding CO)				C_{5+} productivity (mL g_{cat}^{-1} h^{-1})
						CH_4	C_{2-4}	C_{5-11}	C_{12+}	
22Fe3K/$CuAl_2O_4$	320	3	10 000	41.9	10.2	12.5	33.0	48.9	5.6	429.4
22Fe3K/$CuAl_2O_4$(comm.)				30.2	35.5	16.8	47.7	32.9	2.6	145.1

Table S4 Effect of temperature on the catalytic performance of 22Fe3K/$CuAl_2O_4$ as shown in Fig. S14.

Catalyst	Temp. (°C)	P (MPa)	GHSV (mL g_{cat}^{-1} h^{-1})	CO_2 conv. (%)	CO sel. (%)	Hydrocarbon distribution (Excluding CO)				C_{5+} productivity (mL g_{cat}^{-1} h^{-1})
						CH_4	C_{2-4}	C_{5-11}	C_{12+}	
22Fe3K/$CuAl_2O_4$	300	3	10 000	36.5	14.6	14.5	40.8	42.2	2.4	275.5
	320			41.9	10.2	12.5	33.0	48.9	5.6	429.4
	350			46.4	10.9	14.0	30.6	48.6	6.8	479.5
	400			50.3	14.3	27.4	39.8	30.3	2.4	295.8

Table S5 Effect of pressure on the catalytic performance of 22Fe3K/$CuAl_2O_4$ as shown in Fig. S15.

Catalyst	Temp. (°C)	P (MPa)	GHSV (mL g_{cat}^{-1} h^{-1})	CO_2 conv. (%)	CO sel. (%)	Hydrocarbon distribution (Excluding CO)				C_{5+} productivity (mL g_{cat}^{-1} h^{-1})
						CH_4	C_{2-4}	C_{5-11}	C_{12+}	
22Fe3K/$CuAl_2O_4$	320	0.1	10 000	20.8	88.2	29.1	51.2	19.8	-	2.0
		1		30.4	30.3	15.4	45.1	37.4	2.1	163.3
		2		35.5	18.6	13.8	38.7	45.0	2.6	276.8
		3		41.9	10.2	12.5	33.0	48.9	5.6	429.4

Table S6 Effect of the GHSV on the catalytic performance of 22Fe3K/$CuAl_2O_4$ as shown in Fig. S16.

Catalyst	Temp. (°C)	P (MPa)	GHSV (mL g_{cat}^{-1} h^{-1})	CO_2 conv. (%)	CO sel. (%)	Hydrocarbon distribution (Excluding CO)				C_{5+} productivity (mL g_{cat}^{-1} h^{-1})
						CH_4	C_{2-4}	C_{5-11}	C_{12+}	
22Fe3K/$CuAl_2O_4$	320	3	4000	42.0	10.2	15.2	39.0	40.7	5.1	142.9
			10 000	41.9	10.2	12.5	33.0	48.9	5.6	429.4
			15 000	38.1	14.7	14.4	39.7	37.8	8.1	462.2
			20 000	36.8	16.5	14.3	40.4	37.7	7.6	565.0

Table S7 Surface composition of as-synthesized 22Fe3K/$CuAl_2O_4$ determined through EDS mapping (Fig. 3b).

Element	Content	
	wt.%	at.%
Fe	55.3	30.3
K	0.8	0.6
Cu	9.3	4.5
Al	1.8	2.1
O	32.8	62.6

Table S8 Surface composition of the 22Fe3K/$CuAl_2O_4$ catalyst after reduction determined by EDS mapping (Fig. 3f).

Element	Content	
	wt.%	at.%
Fe	20.4	9.5
K	1.6	1.0
Cu	17.8	7.3
Al	24.3	23.5
O	35.9	58.6

Table S9 Surface composition of the 22Fe3K/$CuAl_2O_4$ catalyst after the 40 h reaction determined by EDS mapping (Fig. 3i).

Element	Content	
	wt.%	at.%
Fe	35.3	21.0
K	1.7	1.4
Cu	23.9	12.5
Al	18.9	23.3
O	20.2	41.8